



0D/3D MoS₂-NiS₂/N-doped graphene foam composite for efficient overall water splitting

Panyong Kuang^a, Min He^a, Haiyuan Zou^a, Jiaguo Yu^{a,b,*}, Ke Fan^{a,*}

^a State Key Laboratory of Advanced Technology for Materials Synthesis and Processing, Wuhan University of Technology, Wuhan 430070, PR China

^b Department of Physics, Faculty of Science, King Abdulaziz University, Jeddah 21589, Saudi Arabia

ARTICLE INFO

Keywords:

Three-dimensional
Nitrogen-doped graphene foam
Bimetallic sulfides
Strong chemical interactions
Overall water splitting

ABSTRACT

Electrochemical water splitting is strongly dependent on mass transport and active sites, however, the difficulty in facilitating mass transport and exposing sufficient active sites is the major bottleneck for both half reactions of the overall water splitting, *i.e.*, hydrogen evolution reaction (HER) and oxygen evolution reaction (OER). To address these two issues, a facile and economical strategy is demonstrated for the preparation of the bimetallic sulfides anchored three-dimensional (3D) nitrogen-doped graphene foam (MoS₂-NiS₂/NGF) hybrid for efficient overall water splitting. As a result, strong interactions occur between MoS₂-NiS₂ nanoparticles and NGF with unique 3D interconnected tubular hollow structure, leading to the superior performance towards HER and OER. The overpotential and charge transfer resistance of the hybrid are much lower than those of the bare NGF, MoS₂/NGF, NiS₂/NGF, and physically mixed MoS₂-NiS₂ + NGF, which can be attributed to the synergistic effect of NGF and bimetallic sulfides with hetero interfaces, thus endowing MoS₂-NiS₂/NGF abundant active sites and diversified pathways for highly-efficient transport of mass and electron. This bifunctional catalyst also exhibits excellent overall water splitting capability with a current density of 10 mA cm⁻² at 1.64 V, which provides a platform for the synthesis of large-scale and cost-efficient catalysts for water splitting.

1. Introduction

Electrocatalytic water splitting to produce hydrogen and oxygen is an appealing yet challenging task. The development of the two half reactions of hydrogen evolution reaction (HER) and oxygen evolution reaction (OER) with low overpotential over electrocatalysts is of paramount importance for the successful application of overall water splitting [1–4]. At present, precious noble metal-based electrocatalysts (Pt, RuO₂ and IrO₂) have been regarded as the highly-efficient and ideal HER and OER catalysts to lower the overpotential and reach considerable energy conversion efficiency [5–7]. However, the deficient and high costs are standing in the way of the large-scale applications for these noble metal-based materials. To turn around this adverse situation, massive research on seeking for advanced, economical, and earth-abundant bifunctional electrocatalysts for overall water splitting is underway, which is still a grand challenge thus far.

In this context, some transition-metal sulfides have been widely employed as bifunctional HER and OER electrocatalysts [8–13], simplifying and optimizing the water splitting system, as well as lowering the product costs. Particularly, hybrid of bimetallic sulfides show

superior catalytic performance compared to their monometallic counterparts [14,15]. Much more active sites can be exposed when combining two or more metal species, thus improves the electrochemical reaction kinetics. More importantly, bimetallic sulfides tend to form the heterointerfaces which is able to facilitate the dissociation of H₂O molecules and then boost the electrocatalytic performances, as exemplified by the previous studies reported by our group [16] and others [14,17]. In the effort to achieve higher performance, one effective way recently adopted is to incorporate these transition-metal sulfides with carbon additives, which can improve the conductivity and further facilitate the electrocatalytic activity. Among them, two-dimensional (2D) graphene has been attracting increasing attention [18–24]. However, when compositing 2D graphene with electrocatalysts, one of the major problems is the tendency of the 2D graphene materials to aggregate and/or restack due to the existence of van der Waals interactions and/or strong π - π stacking between the graphene sheets [25]. Such irreversible aggregation and stacking not only hamper the homogeneous dispersion of the hybrid catalysts to lower the quality of the catalyst ink, but also make their surface partially inaccessible to reactants and electrolyte. Moreover, it is also detrimental to the

* Corresponding authors at: State Key Laboratory of Advanced Technology for Materials Synthesis and Processing, Wuhan University of Technology, Wuhan 430070, PR China.

E-mail addresses: jiaguoyu@yahoo.com (J. Yu), kefan@kth.se (K. Fan).

<https://doi.org/10.1016/j.apcatb.2019.04.072>

Received 22 December 2018; Received in revised form 22 March 2019; Accepted 20 April 2019

Available online 25 April 2019

0926-3373/© 2019 Elsevier B.V. All rights reserved.

evolution and release of gas products of electrolysis, forming aggregated bubbles on the surface of electrocatalysts to block active sites from the electrolyte. These structural drawbacks inevitably cause poor conductivity and compromise the electrocatalytic activity. A desirable electrocatalyst should possess not only rich micropores to supply abundant active sites, but also unimpeded channels and high conductivity for improving electron and mass transfer [26]. Therefore, it is necessary to consider the impact of structure on the reaction activity of HER and OER in a rational design for highly active electrocatalysts [27].

Recently, three-dimensional (3D) graphene with interconnected tubular structure has been successfully prepared by various methods, including template-assisted synthesis [28], self-assembly [29–31], and direct deposition [32,33], etc. It has been demonstrated to be a promising additive for electrocatalyst because of its remarkable electrical properties, diversified pore structure, and fast kinetics for mass and electron transfer [31,34]. The high macroporosity of 3D graphene can greatly increase the accessible surface area of the loaded catalysts, provide multiplex electron transfer network, and facilitate the desorption of gas products [35]. These unique properties strongly suggest that 3D graphene is an ideal scaffold for improving the electrocatalytic activity of the supported materials. For example, Zou et al. [36] prepared 2D Ni_xS_y nanowalls decorated 3D nitrogen-doped graphene foam by using the template-assisted method and further employed it as a trifunctional catalyst in unassisted artificial photosynthesis. Zhao et al. [31] reported 3D graphene aerogel supported layered MoS_2 nanosheets catalyst via self-assembly approach, which exhibited high catalytic activity and excellent durability for HER application. Motivated by the above studies, herein, a designed template-assisted method for the fabrication of bimetallic sulfides of MoS_2 and NiS_2 ($\text{MoS}_2\text{-NiS}_2$) anchored 3D nitrogen-doped graphene foam (NGF) as a bifunctional catalyst for HER and OER is reported. We choose melamine sponge as the raw material to prepare NGF due to its low cost and continuous 3D network macroscopic structure. Of special interest to this work, the resulting $\text{MoS}_2\text{-NiS}_2/\text{NGF}$ is capable of fully combining the merits of both 3D graphene networks and bimetallic sulfides, achieving more active sites and lower overpotential than the corresponding counterparts. Such synergistic effect states clearly that strong interactions exist between the components, which ultimately realizes the superb activity and durability for overall water splitting. The results can offer a new methodology for rational design and exploration of highly-efficient electrocatalysts towards water electrolysis.

2. Experimental

2.1. Materials and chemicals

Graphite powders was provided by The Six Element (Changzhou) Materials Technology Co., Ltd. $\text{Na}_2\text{MoO}_4 \cdot 2\text{H}_2\text{O}$, $\text{Ni}(\text{NO}_3)_2 \cdot 6\text{H}_2\text{O}$, $\text{C}_6\text{H}_{12}\text{N}_4$ (hexamethylenetetramine, HMT), $\text{C}_2\text{H}_6\text{O}$ (ethanol), and S powders were purchased from Sinopharm Chemical Reagent Co., Ltd. 5 wt.% Nafion ethanol solution was afforded by Yi Er Sheng (Kunshan) International Trade Co. Ltd. Melamine sponge was purchased from Outlook Company (Chengdu).

2.2. Synthesis of $\text{MoO}_2\text{-Ni}(\text{OH})_2/\text{NGF}$

NGF was firstly prepared through a facile and fast method as reported in our previous work [36]. Briefly, graphene oxide (GO) was prepared by oxidation of natural graphite powders according to a modified Hummers method. Then a pre-cleaned melamine sponge was immersed into the GO suspension (4 mg mL^{-1}) for several times to enhance the absorption and diffusion of GO sheets into the sponge. Subsequently, the GO absorbed melamine sponge was burnt by an alcohol burner for about one minute to remove the melamine template and obtain the NGF. As for the synthesis of $\text{MoO}_2\text{-Ni}(\text{OH})_2/\text{NGF}$,

1.5 mmol $\text{Na}_2\text{MoO}_4 \cdot 2\text{H}_2\text{O}$, 1.5 mmol $\text{Ni}(\text{NO}_3)_2 \cdot 6\text{H}_2\text{O}$, and 1.5 mmol HMT were dissolved into 70 mL distilled water and stirred for 20 min. Then, 1.2 mg NGF was immersed into the above solution and subsequently transferred into a 100 mL Teflon-lined stainless steel autoclave. $\text{MoO}_2\text{-Ni}(\text{OH})_2/\text{NGF}$ was obtained by heating the above solution at 150°C for 6 h. As a control, $\text{MoO}_2\text{-Ni}(\text{OH})_2$ was also synthesized by the same process but without the presence of NGF.

2.3. Synthesis of $\text{MoS}_2\text{-NiS}_2/\text{NGF}$

$\text{MoS}_2\text{-NiS}_2/\text{NGF}$ was obtained through a simple chemical vapor deposition (CVD) method. Briefly, the as-synthesized $\text{MoO}_2\text{-Ni}(\text{OH})_2/\text{NGF}$ and S powders were put at two independent porcelain-boats with 50 mg $\text{MoO}_2\text{-Ni}(\text{OH})_2/\text{NGF}$ and 300 mg S powders at the downstream and upstream side of the furnace, respectively. Then, the furnace was allowed to anneal at 350°C for 1 h with a ramp rate of 2°C min^{-1} under Ar flow to obtain the $\text{MoS}_2\text{-NiS}_2/\text{NGF}$. The weight content of NGF is calculated to be 6.4% according to the inductively coupled plasma atomic emission spectroscopy (ICP-AES) results. Additionally, $\text{MoS}_2\text{-NiS}_2$ counterpart can be obtained by conducting the same sulfuration process for $\text{MoO}_2\text{-Ni}(\text{OH})_2$ but without the presence of NGF.

2.4. Synthesis of MoS_2/NGF and NiS_2/NGF

Typically, 0.3 mmol $(\text{NH}_4)_6\text{Mo}_7\text{O}_{24} \cdot 4\text{H}_2\text{O}$, 12 mmol $\text{CH}_4\text{N}_2\text{S}$, and 23 mg NGF were mixed into 70 mL distilled water and stirred for 30 min, then the mixture solution was transferred into a 100 mL Teflon-lined stainless steel autoclave and heated at 180°C for 12 h to obtain MoS_2/NGF precipitate. As for the synthesis of NiS_2/NGF , $\text{Ni}(\text{OH})_2/\text{NGF}$ was firstly obtained by using the same hydrothermal treatment to $\text{MoO}_2\text{-Ni}(\text{OH})_2/\text{NGF}$ but without the presence of $\text{Na}_2\text{MoO}_4 \cdot 2\text{H}_2\text{O}$. Then, NiS_2/NGF was synthesized by sulfuration of $\text{Ni}(\text{OH})_2/\text{NGF}$, which process was similar to the sulfuration of the above $\text{MoO}_2\text{-Ni}(\text{OH})_2/\text{NGF}$.

2.5. Synthesis of $\text{MoS}_2\text{-NiS}_2/\text{rGO}$ and physically mixed $\text{MoS}_2\text{-NiS}_2 + \text{NGF}$

The synthesis method of $\text{MoS}_2\text{-NiS}_2/\text{rGO}$ was similar to that of the $\text{MoS}_2\text{-NiS}_2/\text{NGF}$, except that NGF was replaced by GO. After hydrothermal treatment, the GO was reduced to rGO. As for the preparation of physically mixed $\text{MoS}_2\text{-NiS}_2 + \text{NGF}$, a certain amount of NGF was physically mixed fully with $\text{MoS}_2\text{-NiS}_2$, and the weight content of NGF was fixed at 6.4%.

More detailed information regarding Materials characterization, Electrode preparation, Electrochemical experiments and Capacitance measurements and comparison of ECSA was presented in Supplementary data.

3. Results and discussion

3.1. Preparation and morphology

The NGF was firstly synthesized using a template-assisted strategy by burning GO-absorbed melamine sponge (ca. $1 \text{ cm} \times 1 \text{ cm} \times 0.5 \text{ cm}$, containing C, H, N, and O elements), which is clearly illustrated in Fig. 1. Scanning electron microscopy (SEM) images of the melamine sponge in Fig. 2a–b show the 3D interconnected macroscopic porous structure constructed of solid melamine fibers (with diameters of $\sim 5 \mu\text{m}$). Such unique network structure is expected to be beneficial to the fast diffusion of electrolyte ions and the release of the gas products of water electrolysis. Fig. 2c–d presents the SEM and transition electron microscopy (TEM) images of the prepared GO sheets with the 2D, thin layer, and large surface area characteristics. After immersing the melamine sponge into the GO suspension adequately, the GO sheets uniformly filled into the space within the melamine sponge and wrapped the fibers (Fig. 2e–f). Finally, the GO absorbed melamine sponge was burnt by an alcohol burner for about one minute to remove the

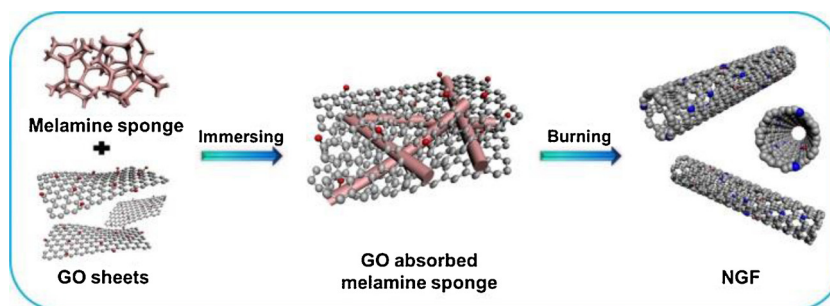


Fig. 1. Schematic illustration for the formation of NGF.

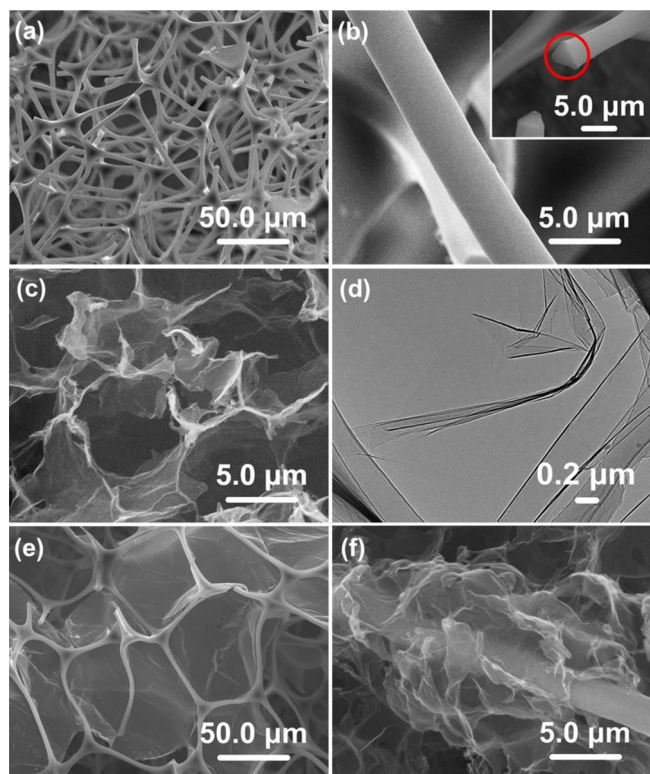


Fig. 2. (a, b) SEM images of melamine. (c) SEM and (d) TEM images of GO sheets. (e, f) SEM images of GO absorbed melamine.

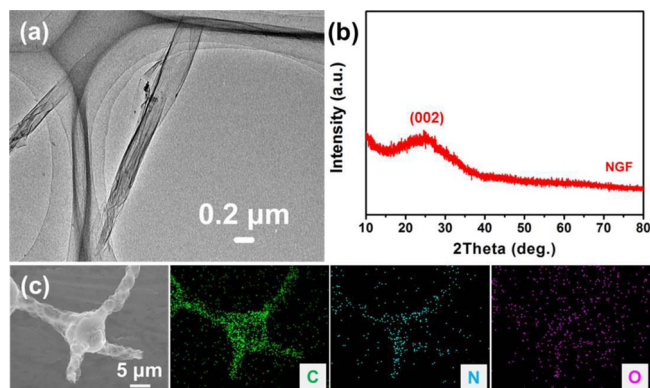


Fig. 3. (a) TEM image, (b) XRD pattern, and (c) EDS mapping images of NGF.

melamine template. As can be seen from the Raman spectra of NGF and melamine (Fig. S1), the several peaks originated from melamine disappeared after burning by alcohol burner [37]. By contrast, only two peaks (D band and G band) derived from graphene were observed for

NGF, indicating the complete removal of melamine. In addition, the greatly increased ratio of D to G band ($I_D : I_G$) for NGF suggests the reduction of GO during burning process (Fig. S2). The TEM image of a piece of broken NGF (Fig. 3a) revealing the thin layer feature of GO sheet. X-ray diffraction (XRD) pattern of NGF (Fig. 3b) presents a broad diffraction peak at $20\text{--}30^\circ$, which is ascribed to the graphite-type carbon with (002) crystal plane [38,39]. Energy-dispersive spectroscopy (EDS) mapping images in Fig. 3c show homogeneously distributed C, O, and N elements in NGF, which can be a strong evidence for the formation of N doping. Besides, Fourier transform infrared spectroscopy (FT-IR) spectra of NGF and GO are displayed in Fig. S3 to further verify the N doping. Furthermore, the negatively charged surface of graphene enables the electrostatic adsorption of Mo^{2+} and Ni^{2+} cations owing to the negative zeta potential (Fig. S4).

Fig. 4a presents the schematic illustration for the synthesis of $\text{MoS}_2\text{-NiS}_2/\text{NGF}$. Fig. S5 shows the optical images of the transformation from bare melamine sponge to $\text{MoS}_2\text{-NiS}_2/\text{NGF}$. NGF was used as the framework for the growing of $\text{MoO}_2\text{-Ni(OH)}_2$ nanowalls through the hydrothermal method and followed anchorage of $\text{MoS}_2\text{-NiS}_2$ nanoparticles via CVD treatment. From Fig. 4b, it can be seen that the NGF maintains the 3D network structure of the GO absorbed melamine precursor. However, the scaffolds become hollow tubular with a diameter of $3\text{--}4\text{ }\mu\text{m}$ (inset, Fig. 4b), which is completely different from the original solid melamine fibers (inset, Fig. 2b). Such unique structure endows NGF with favorable space and superior capability for electrons and ions transfer. It is also observed a highly wrinkled surface of NGF (Fig. 4c) compared to the smooth surface of the initial melamine template (Fig. 2b), which is beneficial to the adsorption of transition metals in the following experiments. $\text{MoO}_2\text{-Ni(OH)}_2$ nanowalls are homogeneously grown on the surface of NGF after hydrothermal treatment, constructing a hierarchical 2D/3D hybrid structure (Fig. 4d–e, Fig. S6–S7). Dramatically, $\text{MoO}_2\text{-Ni(OH)}_2$ nanowalls can be converted to $\text{MoS}_2\text{-NiS}_2$ nanoparticles anchored on NGF after *in situ* sulfuration, as shown in Fig. 4f–g. XRD pattern confirms that $\text{MoO}_2\text{-Ni(OH)}_2/\text{NGF}$ was thoroughly *in situ* transformed to $\text{MoS}_2\text{-NiS}_2/\text{NGF}$ (Fig. 5), which can be well indexed with the MoS_2 (rhombohedral phase, JCPDS No. 37-1492) and NiS_2 (cubic phase, JCPDS No. 65-3325). These $\text{MoS}_2\text{-NiS}_2$ nanoparticles anchored on NGF are supposed to provide a high density of active sites and enhance the electrolyte diffusion, which is indispensable for improving the catalytic activity. In contrast, $\text{MoO}_2\text{-Ni(OH)}_2$ and $\text{MoS}_2\text{-NiS}_2$ are uneven-sized and severely aggregated with the absence of NGF (Fig. 6, Fig. S8–S10), significantly decreasing the contact area of the material with electrolyte and impeding the release of gas products of electrolysis. These results suggest that NGF not only serves as a matrix to grow well-dispersed $\text{MoS}_2\text{-NiS}_2$, but also can facilitate the fast and efficient electron transfer and gas products diffusion.

3.2. Microstructure characterizations

Fig. 7a–b presents a single part of $\text{MoS}_2\text{-NiS}_2/\text{NGF}$, clearly

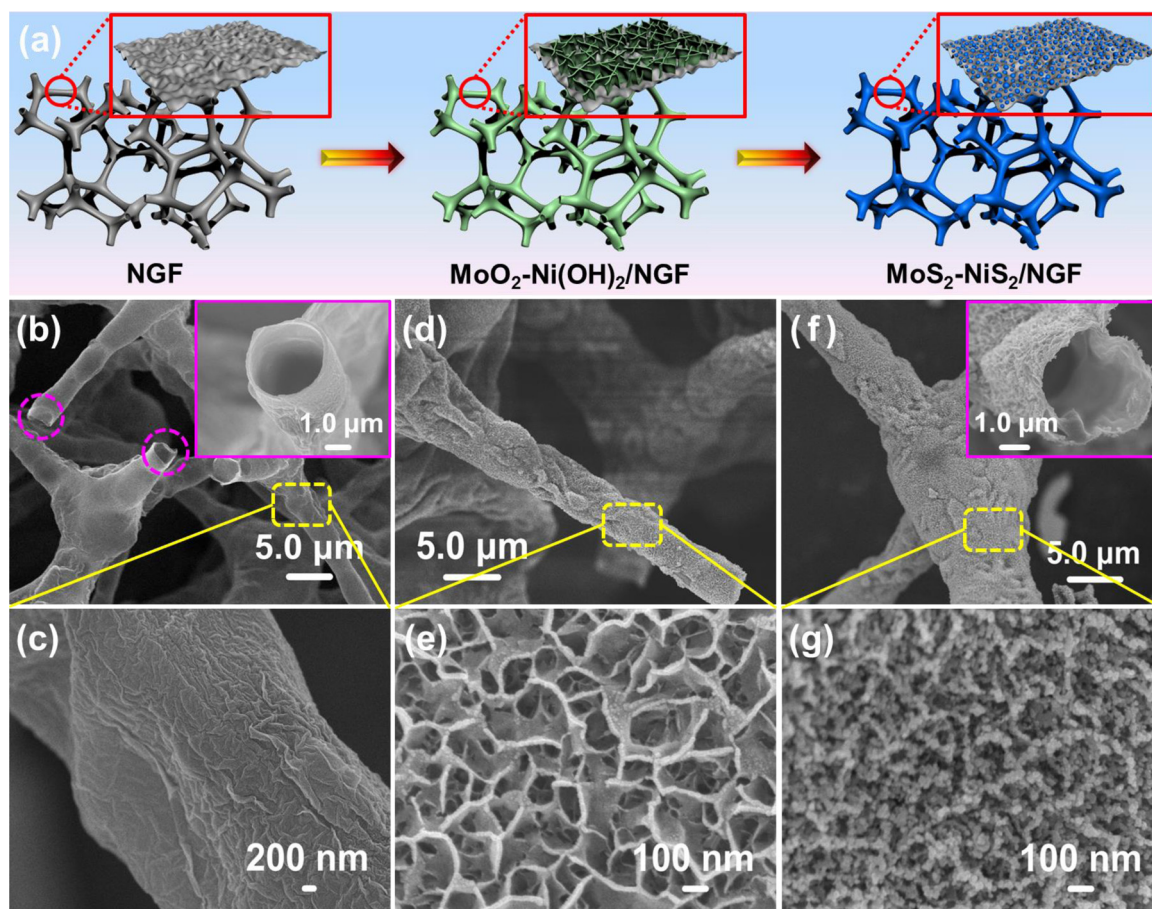


Fig. 4. (a) Schematic illustration for the synthesis of $\text{MoS}_2\text{-NiS}_2/\text{NGF}$. SEM images of (b, c) NGF, (d, e) $\text{MoO}_2\text{-Ni(OH)}_2/\text{NGF}$, and (f, g) $\text{MoS}_2\text{-NiS}_2/\text{NGF}$.

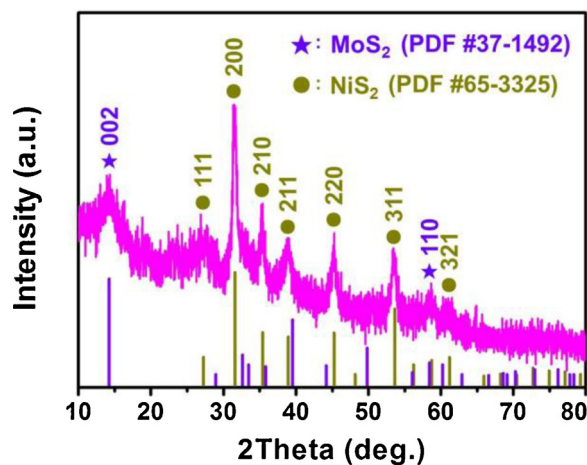


Fig. 5. XRD pattern of $\text{MoS}_2\text{-NiS}_2/\text{NGF}$.

displaying the tubular structure and consistent with the observation of NGF in the aforementioned characterizations. According to the results of SEM (Fig. 4) and TEM images, the NGF serves as 3D scaffold to support the distribution of OD $\text{MoS}_2\text{-NiS}_2$ nanoparticles, forming the OD/3D $\text{MoS}_2\text{-NiS}_2/\text{NGF}$ structure. Fig. 7b–c display the TEM images of $\text{MoS}_2\text{-NiS}_2/\text{NGF}$ fragments. These $\text{MoS}_2\text{-NiS}_2$ nanoparticles are well-distributed and strongly anchored on the NGF surface. The strong interactions between $\text{MoS}_2\text{-NiS}_2$ and NGF could favour the electron transfer, thus generate a predictable positive synergistic effect. Fig. S11 presents the selected area electron diffraction (SAED) pattern of $\text{MoS}_2\text{-NiS}_2/\text{NGF}$, revealing the polycrystalline feature due to the coexistence

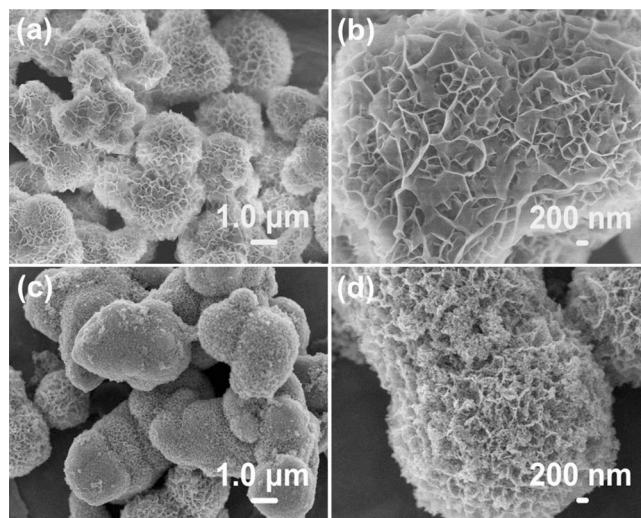


Fig. 6. SEM images of the counterparts of (a, b) $\text{MoO}_2\text{-Ni(OH)}_2$ and (c, d) $\text{MoS}_2\text{-NiS}_2$.

of MoS_2 and NiS_2 . The high-resolution TEM (HRTEM) images (Fig. 7e–f) reveal several-nanometer-size MoS_2 and NiS_2 nanoparticles, where the lattice spacing of 0.61 and 0.25 nm can be indexed to (002) and (210) planes of MoS_2 and NiS_2 , respectively. It is noteworthy that hetero-interface is formed between the (002) plane of MoS_2 and (210) plane of NiS_2 (Fig. 7f). According to our previous experimental and theoretical studies, the heterointerface would serve as the dissociation site for H_2O , where H is inclined to be adsorbed by MoS_2 and OH will be intensely

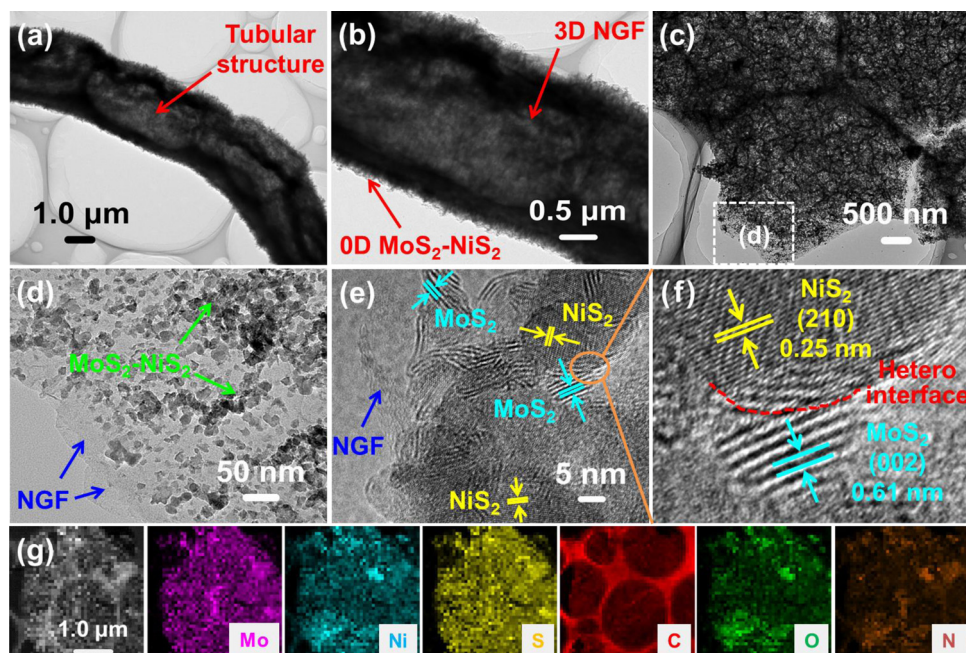


Fig. 7. (a–d) TEM images, (e, f) HRTEM images, and (g) EDS mapping images of MoS₂-NiS₂/NGF.

adsorbed by NiS₂. As a result, the Gibbs free energies of the intermediates are efficiently decreased, facilitating the dissociation of H–O bond of the H₂O [16]. Besides, other researches also proved that the heterointerface formed between bimetallic sulfides plays a vital role in boosting electrocatalytic activity [14,17]. Moreover, the EDS mapping images in Fig. 7g show that the Mo, Ni, and S elements derived from OD MoS₂-NiS₂ nanoparticles homogeneously distributed over the 3D NGF substrate.

3.3. XPS, Raman and FT-IR analysis

Fig. S12a presents the X-ray photoelectron spectroscopy (XPS) survey spectrum of MoS₂-NiS₂/NGF, containing Mo, Ni, S, C, N, and O elements. Because of the uniform and full coverage of MoS₂-NiS₂ nanoparticles on NGF surface, the intensities of C 1s and N 1s peaks in MoS₂-NiS₂/NGF decrease dramatically compared with those of the bare NGF (Fig. S12b). Fig. 8a–e show the high-resolution XPS spectra of Mo 3d, Ni 2p, S 2p, C 1s, and N 1s for MoS₂-NiS₂/NGF. The XPS spectrum of Mo 3d (Fig. 8a) exhibits two characteristic peaks of Mo 3d_{3/2} (232.6 eV) and Mo 3d_{5/2} (229.4 eV), associating with the Mo⁴⁺ oxidation state in MoS₂-NiS₂/NGF [40]. Moreover, a weak neighboring S 2s peak is derived from Mo–S and Ni–S bonds, respectively [41–43]. In the XPS spectrum of Ni 2p (Fig. 8b), the strong 2p_{1/2} and 2p_{3/2} peaks located at 872.8 and 855.3 eV along with two satellite peaks are characteristics of Ni²⁺ [44–46]. Meanwhile, the S 2p XPS spectrum in Fig. 8c suggests the S^{2–} species in basal plane positions or bridging S₂^{2–} in terminal sites [47–49]. The C 1s XPS spectrum (Fig. 8d) consists four peaks centered at 284.3, 285.0, 286.1, and 288.4 eV, attributing to the C–C/C=C, C–N, C–O, and C=O bonds, respectively [50–52]. Moreover, the deconvoluted N 1s XPS spectrum (Fig. 8e) reveals graphitic N (401.6 eV), pyrrolic N (399.4 eV), pyridinic N (398.2 eV), and an accompanying minor Mo 3p_{3/2} species (395.5 eV), suggesting the successful incorporation of N into the graphene (The bonding configurations of these N functionalities are schematically shown in Fig. 8f) [53–55]. Furthermore, N doping can not only provide more active sites for graphene, but also strengthen the interactions between carbon matrix and guest materials [56,57], thus improves the electron transfer kinetics in MoS₂-NiS₂/NGF. Interestingly, the binding energies of Mo 3d and Ni 2p for MoS₂-NiS₂/NGF shift to higher values compared to those of MoS₂-NiS₂ (Fig. 9a–b and Table S1); contrarily, negative shifts of C 1s and N

1s binding energy occurred for MoS₂-NiS₂/NGF compared to those of bare NGF (Fig. 9c–d), suggesting that MoS₂-NiS₂ can form strong chemical interactions and electronic coupling with NGF. To further verify the chemical interactions of MoS₂-NiS₂ anchored NGF, both Raman and FT-IR spectra were recorded. As shown in Fig. 10a, the Raman spectrum of NGF shows two intense peaks located at 1331.2 and 1595.9 cm^{–1}, corresponding to the D band (sp³ hybridized carbon atoms of graphene from disorder, edges, and defects) and G band (vibration of sp² carbon atoms in ideal graphene layer) [58], respectively. Compared with the bare NGF, MoS₂-NiS₂/NGF shows distinguished blue-shift of D (1329.6 cm^{–1}) and G (1583.7 cm^{–1}) bands, suggesting the chemical interactions and electron transfer between MoS₂-NiS₂ and NGF. It is found that the MoS₂-NiS₂/NGF has a higher I_D (intensity of D band)/I_G (intensity of G band) ratio of 1.16 than that of the bare NGF (I_D/I_G = 1.10), suggesting the increment of defects, edges, and disorder by the removal of oxygen-containing functional groups after hydrothermal and sulfuration treatments, which provides more active sites for enhanced electrocatalytic activity. Consistent with Raman analysis, the FT-IR spectrum also corroborates the strong interactions in MoS₂-NiS₂/NGF, as presented in Fig. 10b. One new peak appeared at 623 cm^{–1} is identified for the obtained MoS₂-NiS₂/NGF compared with MoS₂-NiS₂ and NGF, clearly corresponding to the C–S stretches [58,59]. In addition, we also performed the FT-IR spectra of MoS₂-NiS₂/rGO and physically mixed MoS₂-NiS₂ + NGF (Fig. 10c), the peak of the C–S stretches is still clearly identified for MoS₂-NiS₂/rGO while it is absent for the latter. Therefore, the results of XPS, Raman, and FT-IR provide unambiguous proof of the strong interactions between MoS₂-NiS₂ and NGF, which would be responsible for the enhanced electrocatalytic performances of HER, OER, and overall water splitting applications.

3.4. Hydrogen evolution reaction

To find the application of MoS₂-NiS₂/NGF in the electrolysis of water, the HER measurements were tested with a scan rate of 5 mV s^{–1} in 1.0 M KOH electrolyte using a standard three-electrode configuration. As shown in Fig. 11a, excellent catalytic activity was endowed for MoS₂-NiS₂/NGF, a significant cathodic current density was observed with increasing the applied overpotential, accompanied by rapid evolution and release of a large amount of hydrogen bubbles. Furthermore, the overpotential for MoS₂-NiS₂/NGF to attain -10 mA cm^{–2} catalytic

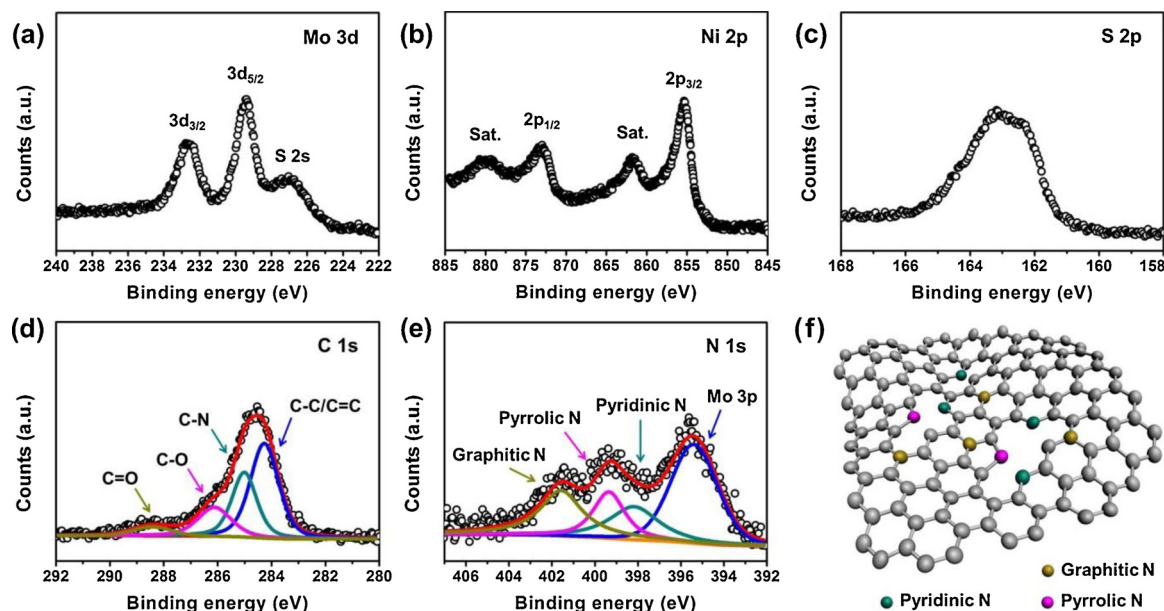
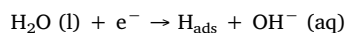


Fig. 8. High-resolution XPS spectra of (a) Mo 3d, (b) Ni 2p, (c) S 2p, (d) C 1s, and (e) N 1s for MoS₂-NiS₂/NGF. (f) Schematic of the bonding configurations of N functionalities.

current density (η_{10}) is 172 mV, which is obviously lower than that of MoS₂-NiS₂ (225 mV) (Fig. 11b). In sharp contrast, negligible current densities were observed for bare NGF, MoO₂-Ni(OH)₂, and MoO₂-Ni(OH)₂/NGF in the whole potential range (Fig. 11a and S13), suggesting that the additive of carbon material and sulfuration treatment play important roles toward the enhanced electrocatalytic activity. The overpotential of MoS₂-NiS₂/NGF at current density of -10 mA cm^{-2} is also superior to those of other noble metal-free HER catalysts (Table S2) [42,47,60–63]. Such high catalytic activity of MoS₂-NiS₂/NGF makes it be a promising alternative to hydrogen evolution electrocatalyst for feasible industrial alkaline water splitting. Onset overpotential of the catalyst can be defined in different ways to indicate the starting of water electrolysis. Here, we define the overpotential as the onset

overpotential at -1 mA cm^{-2} catalytic current density. As presented in Fig. 11b, bearable onset overpotential of 68 mV is achieved on MoS₂-NiS₂/NGF, which is significantly lower than those of MoS₂-NiS₂ (119 mV) and NGF (487 mV). Moreover, MoS₂-NiS₂/NGF yields a Tafel slope of 70 mV dec^{-1} , much lower than those of MoS₂-NiS₂ (97 mV dec^{-1}) and NGF (364 mV dec^{-1}) (Fig. 11c). The small Tafel slope of MoS₂-NiS₂/NGF suggests a facile kinetics of hydrogen generation. Note that three major pathways are involved for hydrogen evolution in alkaline condition [1,64]:



(Volmer pathway, Tafel slope of 120 mV dec^{-1}) (1)

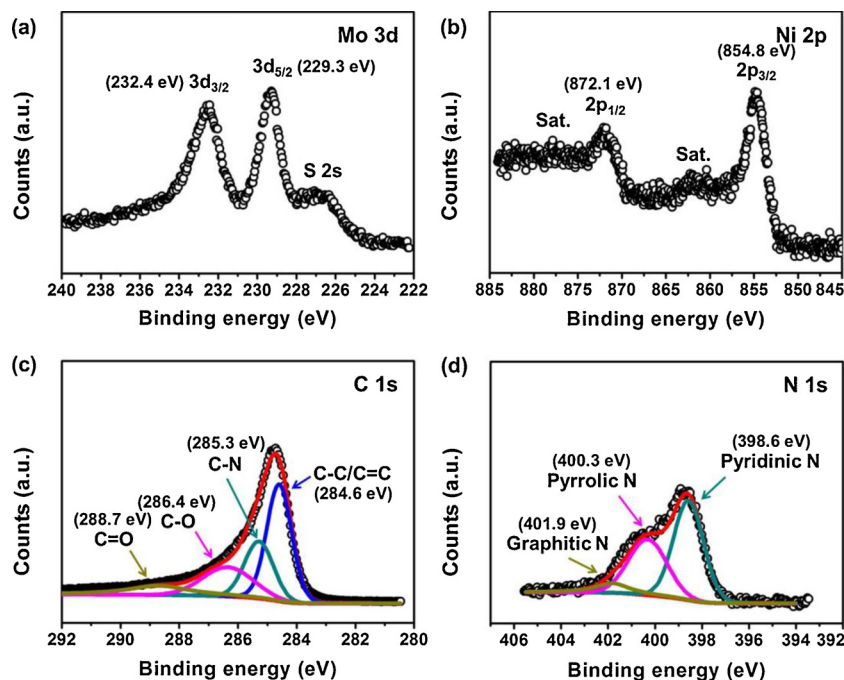
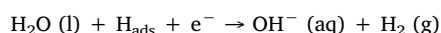


Fig. 9. High-resolution XPS spectra of (a) Mo 3d and (b) Ni 2p for MoS₂-NiS₂, (c) C 1s and (d) N 1s for NGF.

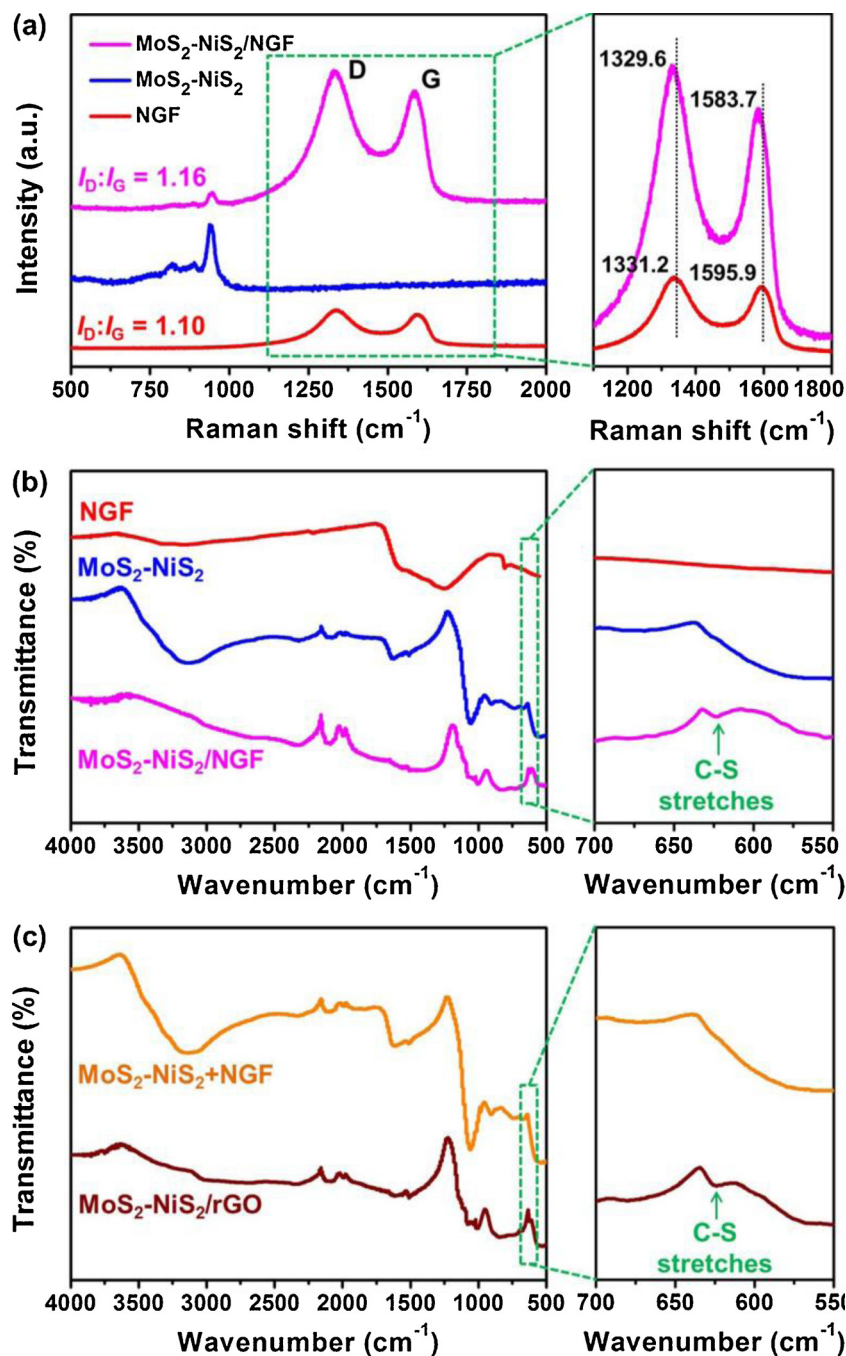


Fig. 10. (a) Raman and (b) FT-IR spectra of MoS₂-NiS₂/NGF, MoS₂-NiS₂, and NGF. (c) FT-IR spectra of MoS₂-NiS₂+NGF and MoS₂-NiS₂/rGO.

(Heyrovsky pathway, Tafel slope of 40 mV dec⁻¹) (2)



(Tafel pathway, Tafel slope of 30 mV dec⁻¹) (3)

where H_{ads} indicates one H atom adsorbed on the active site of catalyst. Generally, water molecules are initially adsorbed on the surface of catalyst. This procedure can be followed by coupling H_{ads} with another H atom and electron to form and release H₂ (Volmer-Heyrovsky pathway, Eqs. (1) and (2)) or directly combining two H_{ads} to generate one H₂ molecule (Volmer-Tafel pathway, Eqs. (1)–(3)). In our case, MoS₂-NiS₂/NGF exhibits Tafel slope of 70 mV dec⁻¹, suggesting the likely Volmer-Heyrovsky pathway for HER process.

Fig. 11d displays the electrochemical impedance spectroscopy (EIS)

of samples at the overpotential of 300 mV in 1.0 M KOH. In low-frequency region, a noticeably reduced semicircle for MoS₂-NiS₂/NGF is observed compared to MoS₂-NiS₂ and NGF, indicating the promoted interfacial reaction kinetics and facilitated charge transfer in MoS₂-NiS₂/NGF, which is responsible for the higher HER catalytic performance. It is reported that the charge transfer resistance can be greatly reduced by incorporating the catalysts with high conductivity matrices, such as carbon nanotubes [65] and graphene [66]. Therefore, the enhanced electrical conductivity of MoS₂-NiS₂/NGF can be attributed to the synergistic effect between MoS₂-NiS₂ and NGF, as well as the 3D interconnected macroscopic porous structure of NGF. Moreover, the cyclic voltammetry (CV) tests were conducted to determine the electrochemically active surface area (ECSA) of samples. At each scan rate, MoS₂-NiS₂/NGF provides much higher current densities than those of MoS₂-NiS₂ and NGF (Fig. 11e–f, Fig. S14), implying a much larger

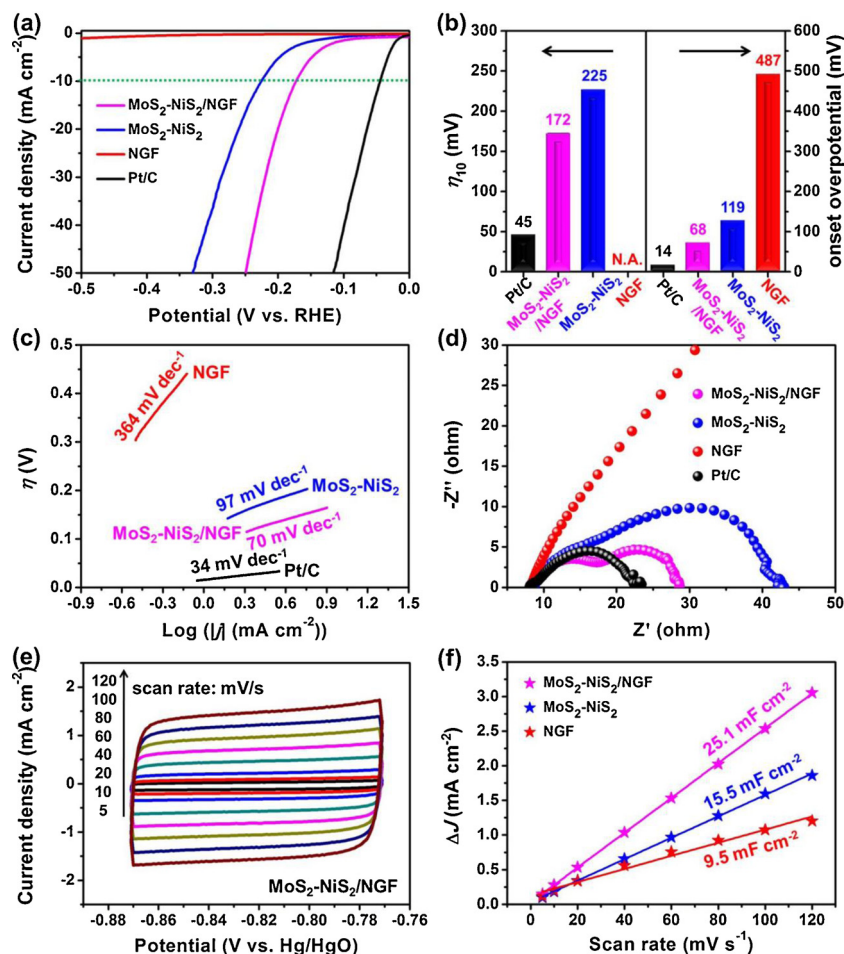


Fig. 11. (a) Polarization curves of $\text{MoS}_2\text{-NiS}_2/\text{NGF}$, $\text{MoS}_2\text{-NiS}_2$, NGF, and Pt/C electrodes for HER measured at a scan rate of 5 mV s^{-1} in 1.0 M KOH. (b) Corresponding η_{10} and onset overpotential values and (c) corresponding Tafel slopes. (d) Nyquist plots with an overpotential of 300 mV in 1.0 M KOH. (e) Typical cyclic voltammogram (CV) curves of $\text{MoS}_2\text{-NiS}_2/\text{NGF}$ electrode in 1.0 M KOH with different scan rates. (f) Differences in current density ($\Delta J = J_a - J_c$) of $\text{MoS}_2\text{-NiS}_2/\text{NGF}$, $\text{MoS}_2\text{-NiS}_2$, and NGF plotted against scan rates.

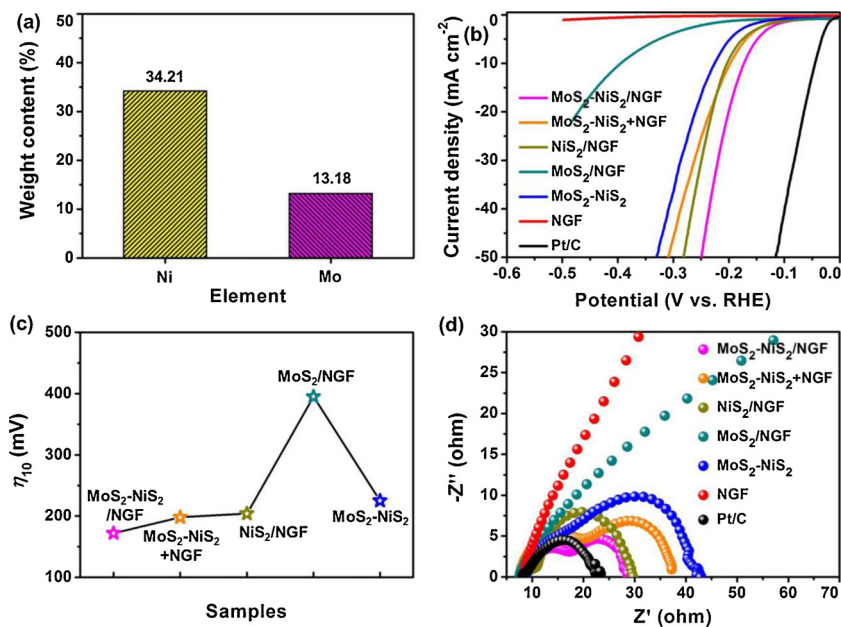


Fig. 12. (a) ICP-AES results of $\text{MoS}_2\text{-NiS}_2/\text{NGF}$. (b) Polarization curves of $\text{MoS}_2\text{-NiS}_2/\text{NGF}$, $\text{MoS}_2\text{-NiS}_2 + \text{NGF}$, NiS_2/NGF , MoS_2/NGF , $\text{MoS}_2\text{-NiS}_2$, NGF, and Pt/C for HER in 1.0 M KOH. (c) Overpotential at 10 mA cm^{-2} obtained on different samples. (d) Nyquist plots of $\text{MoS}_2\text{-NiS}_2/\text{NGF}$, $\text{MoS}_2\text{-NiS}_2 + \text{NGF}$, NiS_2/NGF , MoS_2/NGF , $\text{MoS}_2\text{-NiS}_2$, NGF, and Pt/C for HER with an overpotential of 300 mV in 1.0 M KOH.

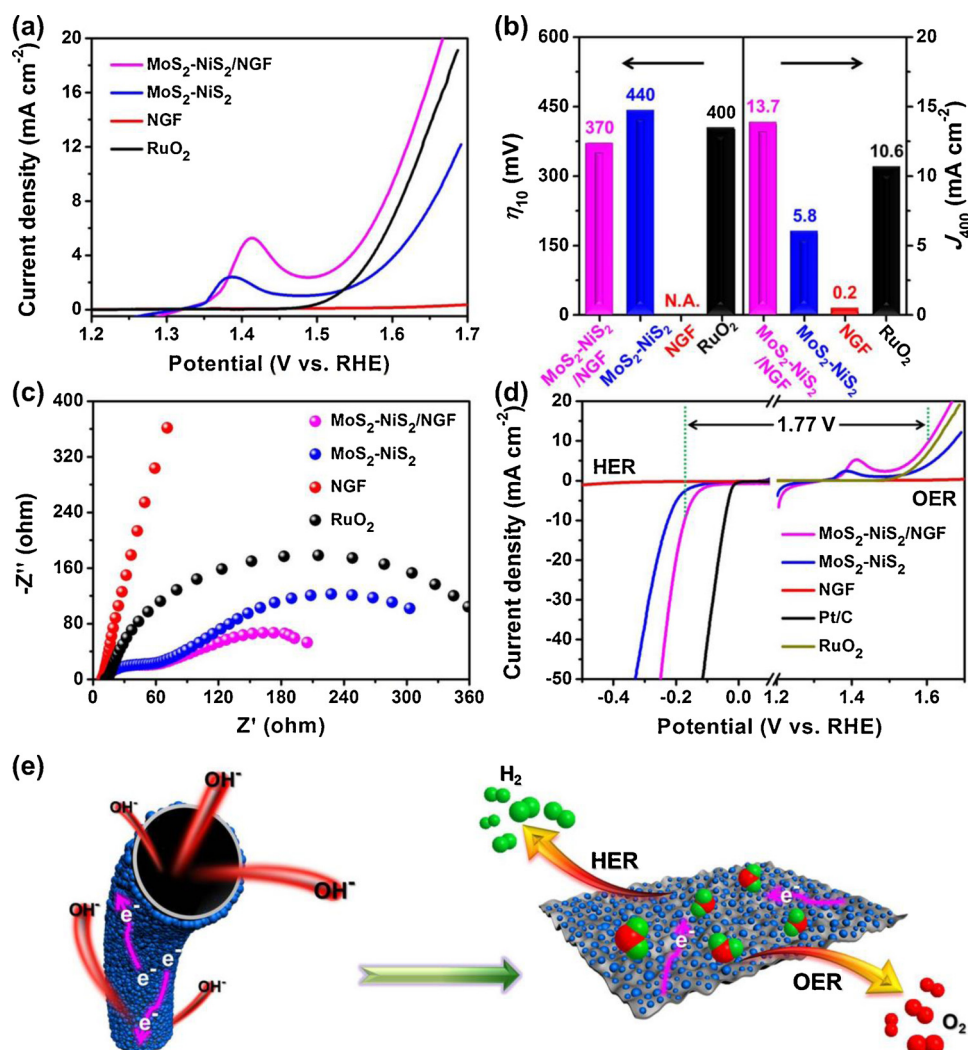


Fig. 13. (a) Polarization curves of MoS₂-NiS₂/NGF, MoS₂-NiS₂, NGF, and RuO₂ electrodes for OER measured at a scan rate of 5 mV s⁻¹ in 1.0 M KOH. (b) Corresponding η_{10} and J_{400} values. (c) Nyquist plots with an overpotential of 350 mV in 1.0 M KOH. (d) Polarization curves of MoS₂-NiS₂/NGF, MoS₂-NiS₂, NGF, Pt/C, and RuO₂ in 1.0 M KOH for HER and OER. (e) Illustration showing the HER and OER processes on MoS₂-NiS₂/NGF.

accessible electrochemical surface area and more exposed reactive sites of the MoS₂-NiS₂/NGF. In order to clarify the synergistic effect of MoS₂-NiS₂ and 3D NGF, we prepared MoS₂/NGF, NiS₂/NGF, and physically mixed MoS₂-NiS₂ + NGF counterparts (6.4 wt.% of NGF, according to the results of ICP-AES (Fig. 12a)) and tested their HER performances under identical conditions. As shown in Fig. 12b–d, MoS₂-NiS₂/NGF exhibits both lower overpotential and charge transfer resistance compared to MoS₂/NGF, NiS₂/NGF, and physically mixed MoS₂-NiS₂ + NGF samples, which further verifies the advantages of the synergistic effect in MoS₂-NiS₂ and NGF. The heterointerfaces of bimetallic sulfides facilitate the dissociation of H₂O molecules and promote the reaction kinetics. Meanwhile, the MoS₂-NiS₂ nanoparticles strongly anchored on NGF and the distinctive 3D interconnected tubular hollow structure significantly accelerate the transfer of electrons and diffusion of electrolyte and gasses. Furthermore, the synergistic effect also benefits the long-term durability. As shown in Fig. S15, the required overpotential of MoS₂-NiS₂/NGF only shows a slight increase at the fixed catalytic current density of -10 mA cm⁻² after a long-term electrolysis, indicating its good durability for hydrogen evolution in alkaline medium.

3.5. Oxygen evolution reaction

The other half reaction of the overall water splitting, OER catalytic activity of MoS₂-NiS₂/NGF was next assessed in the same alkaline

electrolyte to show its capacity as a dual role. As shown in Fig. 13a–b, the bare NGF shows negligible catalytic activity toward OER. MoS₂-NiS₂/NGF exhibits much lower overpotential of 370 mV to attain the current density of 10 mA cm⁻² than that of MoS₂-NiS₂ (440 mV) and RuO₂ (400 mV). Moreover, at the same overpotential of 400 mV, MoS₂-NiS₂/NGF displays a current density of 13.7 mA cm⁻², which is 2.36 and 1.29 times higher than that of MoS₂-NiS₂ and RuO₂. Fig. 13c presents the Nyquist plots of the samples, where MoS₂-NiS₂/NGF exhibits much smaller semicircle than other samples, suggesting its inherent excellent electron transfer ability and facile OER kinetics. Furthermore, the Faradaic efficiency (Φ) of MoS₂-NiS₂/NGF was calculated to be 97%, suggesting that the detected oxidation current is mainly attributed to OER process with four-electron pathway. Fig. 13d displays the integration of the HER and OER curves of the samples. MoS₂-NiS₂/NGF affords current density of 10 mA cm⁻² at a theoretical potential of 1.77 V, which is relatively higher than Pt/C||RuO₂ (1.68 V) but much lower than MoS₂-NiS₂ (1.90 V). The above mentioned excellent HER and OER performance unequivocally corroborate the advantages of the 3D interconnected tubular structure of the MoS₂-NiS₂/NGF sample, which significantly promotes the three-phase reactions (electrodes, electrolyte, and H₂ and O₂ products). As illustrated in Fig. 13e, the 3D hollow tube structure guarantees abundant active sites, and diverse pathways for fast and efficient transport of electrolyte and gases. In addition, the intimate contact of MoS₂-NiS₂ and NGF causes the

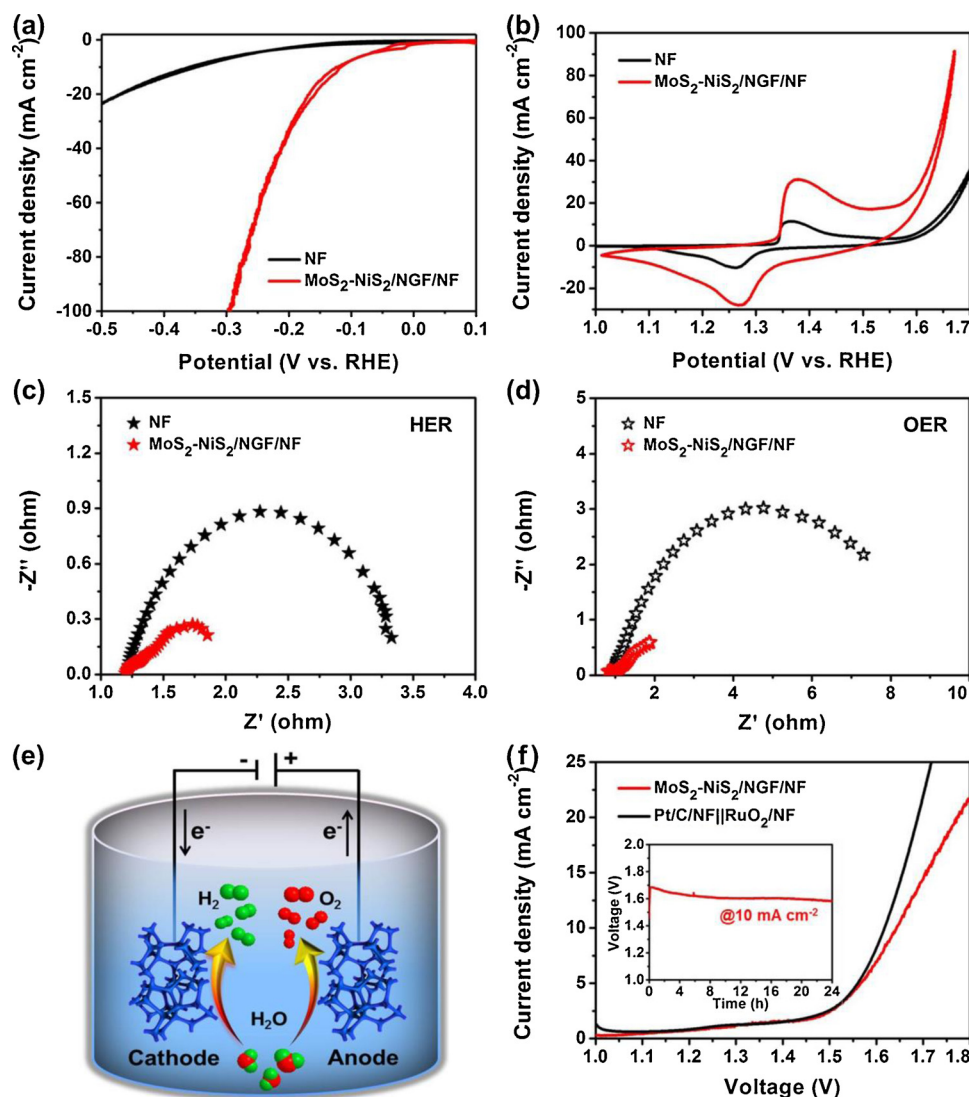


Fig. 14. CV curves of MoS₂-NiS₂/NGF/NF and NF electrodes for (a) HER and (b) OER measured at a scan rate of 5 mV s⁻¹ in 1.0 M KOH, respectively. Nyquist plots of MoS₂-NiS₂/NGF/NF and NF electrodes measured in 1.0 M KOH with an overpotential of (c) 300 mV for HER and (d) 350 mV for OER, respectively. (e) Schematic diagram of the two-electrode water electrolysis device. (f) Polarization curves of two-electrode overall water splitting using MoS₂-NiS₂/NGF/NF as both anode and cathode at a scan rate of 5 mV s⁻¹ in 1.0 M KOH. Inset: galvanostatic measurement of the MoS₂-NiS₂/NGF/NF performed at current density of 10 mA cm⁻² in 1.0 M KOH.

synergistic effect, which enables fast electron transfer and should be another indispensable factor for the excellent catalytic performances.

3.6. Overall water splitting

To further apply the catalysts to large-scale applications, MoS₂-NiS₂/NGF loaded on nickel foam (MoS₂-NiS₂/NGF/NF) electrode was firstly used as both the cathode and anode for HER and OER in three-electrode configuration, respectively. For comparison, the catalytic activity of bare NF was tested. Fig. 14a presents the CV curves of MoS₂-NiS₂/NGF/NF and NF for HER. It can be observed that MoS₂-NiS₂/NGF/NF exhibits superior HER catalytic activity reaching a current density of 10 mA cm⁻² at a low overpotential of 116 mV, whereas a much higher overpotential (360 mV) is required for the bare NF. Moreover, the current density at overpotential of 300 mV is 105 mA cm⁻² for MoS₂-NiS₂/NGF/NF, which is 16 folds higher than that of the bare NF. The OER activity of MoS₂-NiS₂/NGF/NF in alkaline environment was also investigated. As displayed in Fig. 14b, MoS₂-NiS₂/NGF/NF is also capable of catalyzing OER to drive a current density of 10 mA cm⁻² with overpotential of 340 mV, while the bare NF has a poor OER activity. The Nyquist plots for HER and OER clearly demonstrate the greatly decreased electron transfer resistance of MoS₂-NiS₂/NGF/NF (Fig. 14c–d), which ultimately leads to the enhanced electrocatalytic activity. In addition, we further performed the long-term stability tests of MoS₂-NiS₂/NGF/NF electrode for HER and OER under different

current densities (Fig. S16). The almost constant overpotential of each applied current density demonstrates the satisfactory durability of MoS₂-NiS₂/NGF/NF in the alkaline solution. On the basis of the above results, we would reasonably conclude that MoS₂-NiS₂/NGF/NF can be used as HER and OER bifunctional electrodes for overall water splitting in the strong alkaline environment. Therefore, a two-electrode cell using MoS₂-NiS₂/NGF/NF as both cathode and anode was constructed to better realize the practical application (Fig. 14e). As shown in Fig. 14f, the electrolytic cell needs 1.64 V to achieve current density of 10 mA cm⁻², which is comparable to that of Pt/C/NF||RuO₂/NF couple (1.61 V), and close to or even smaller than those of other transition-metal and/or carbon-based bifunctional catalysts (Table S3) [60–62,67–70]. Such high performance is important for the potential large-scale production with low cost and makes MoS₂-NiS₂/NGF/NF a very promising alternative of non-precious catalysts towards overall water splitting. In addition, MoS₂-NiS₂/NGF/NF catalyst is highly-stable for long-term overall water splitting test under the current density of 10 mA cm⁻² (inset of Fig. 14f, Fig. S17, Video S1), suggesting the excellent stability of bifunctional MoS₂-NiS₂/NGF/NF towards water electrolysis. These results support the potential of MoS₂-NiS₂/NGF/NF electrode as a competitive candidate of noble metal-based catalysts in economic and efficient water electrolysis.

4. Conclusions

In summary, we have prepared bimetallic sulfides nanoparticles anchored 3D nitrogen-doped graphene foam (MoS₂-NiS₂/NGF) as a bifunctional electrocatalyst in strong alkaline solution for overall water splitting. Benefiting from the synergistic effect of bimetallic sulfides and NGF and the unique 3D interconnected tubular structure, MoS₂-NiS₂/NGF affords not only abundant active sites, but also diversified pathways for fast and sufficient transport of mass and electrons. MoS₂-NiS₂/NGF delivers a current density of 10 mA cm⁻² at the overpotential of 172 mV for HER and 370 mV for OER in 1.0 M KOH on simple glassy carbon electrode. Furthermore, when used in an alkaline water electrolyzer, the nonprecious-metal MoS₂-NiS₂/NGF on nickel foam produces vigorous and continuous evolution of H₂ and O₂ at a current density of 10 mA cm⁻² under a cell voltage of 1.64 V. The excellent bifunctional activity of our electrocatalyst demonstrates that such MoS₂-NiS₂ anchored 3D NGF is a promising candidate for cost-efficient and large-scale solar-to-hydrogen generation by overall water splitting.

Acknowledgements

This work was partially supported by National Natural Science Foundation of China (U1705251, 21433007, and 51772234), National Key Research and Development Program of China (2018YFB1502001), Innovative Research Funds of SKLWUT (2017-ZD-4), and National Postdoctoral Program for Innovative Talents (BX20180231).

Appendix A. Supplementary data

Supplementary material related to this article can be found, in the online version, at doi:<https://doi.org/10.1016/j.apcatb.2019.04.072>.

References

- [1] V. Vij, S. Sultan, A.M. Harzandi, A. Meena, J.N. Tiwari, W.-G. Lee, T. Yoon, K.S. Kim, *ACS Catal.* 7 (2017) 7196–7225.
- [2] K. Fan, Y. Ji, H. Zou, J. Zhang, B. Zhu, H. Chen, Q. Daniel, Y. Luo, J. Yu, L. Sun, *Angew. Chem. Int. Ed.* 56 (2017) 3289–3293.
- [3] D. Jang, S. Lee, S. Kim, K. Choi, S. Park, J. Oh, S. Park, *ChemNanoMat* 4 (2018) 118–123.
- [4] A. Sivanantham, S. Shanmugam, *Appl. Catal. B: Environ.* 203 (2017) 485–493.
- [5] S. Lu, X. Shang, L. Zhang, B. Dong, W. Gao, F. Dai, B. Liu, Y. Chai, C. Liu, *Appl. Surf. Sci.* 445 (2018) 445–453.
- [6] X. Liu, P. Wang, Q. Zhang, B. Huang, Z. Wang, Y. Liu, Z. Zheng, Y. Dai, X. Qin, X. Zhang, *Appl. Surf. Sci.* 459 (2018) 422–429.
- [7] J. Chang, Q. Lv, G. Li, J. Ge, C. Liu, W. Xing, *Appl. Catal. B: Environ.* 204 (2017) 486–496.
- [8] G.-F. Chen, T.Y. Ma, Z.-Q. Liu, N. Li, Y.-Z. Su, K. Davey, S.-Z. Qiao, *Adv. Funct. Mater.* 26 (2016) 3314–3323.
- [9] A. Chen, R. Cui, Y. He, Q. Wang, J. Zhang, J. Yang, X. Li, *Appl. Surf. Sci.* 411 (2017) 210–218.
- [10] Y. Chen, S. Xu, Y. Li, R.J. Jacob, Y. Kuang, B. Liu, Y. Wang, G. Pastel, L.G. Salamanca-Riba, M.R. Zachariah, L. Hu, *Adv. Energy Mater.* 7 (2017) 1700482.
- [11] J. Yu, Y. Du, Q. Li, L. Zhen, V.P. Dravid, J. Wu, C. Xu, *Appl. Surf. Sci.* 465 (2019) 772–779.
- [12] S. Wang, L. Xu, W. Lu, *Appl. Surf. Sci.* 457 (2018) 156–163.
- [13] C.X. Zhang, S. Bhoyate, P.K. Kahol, K. Siam, T.P. Poudel, S.R. Mishra, F. Perez, A. Gupta, G. Gupta, R.K. Gupta, *ChemNanoMat* 4 (2018) 1240–1246.
- [14] J. Zhang, T. Wang, D. Pohl, B. Rellinghaus, R. Dong, S. Liu, X. Zhuang, X. Feng, *Angew. Chem. Int. Ed.* 55 (2016) 6702–6707.
- [15] Y.-R. Liu, X. Shang, W.-K. Gao, B. Dong, J.-Q. Chi, X. Li, K.-L. Yan, Y.-M. Chai, Y.-Q. Liu, C.-G. Liu, *Appl. Surf. Sci.* 412 (2017) 138–145.
- [16] P. Kuang, T. Tong, K. Fan, J. Yu, *ACS Catal.* 7 (2017) 6179–6187.
- [17] Y. Yang, K. Zhang, H. Lin, X. Li, H.C. Chan, L. Yang, Q. Gao, *ACS Catal.* 7 (2017) 2357–2366.
- [18] A. Vasileff, S. Chen, S.Z. Qiao, *Nanoscale Horiz.* 1 (2016) 41–44.
- [19] H. Meng, K. Fan, J. Low, J. Yu, *Dalton Trans.* 45 (2016) 13717–13725.
- [20] X. Li, J. Yu, S. Wageh, A.A. Al-Ghamdi, J. Xie, *Small* 12 (2016) 6640–6696.
- [21] J. Li, Z. Zhao, Y. Ma, Y. Qu, *ChemCatChem* 9 (2017) 1554–1568.
- [22] Q. Xiang, J. Yu, M. Jaroniec, *J. Am. Chem. Soc.* 134 (2012) 6575–6578.
- [23] Q. Li, X. Li, S. Wageh, A.A. Al-Ghamdi, J. Yu, *Adv. Energy Mater.* 5 (2015) 1500010.
- [24] Q. Xiang, J. Yu, M. Jaroniec, *Chem. Soc. Rev.* 41 (2012) 782–796.
- [25] S. Mao, G. Lu, J. Chen, *Nanoscale* 7 (2015) 6924–6943.
- [26] J.-C. Li, P.-X. Hou, S.-Y. Zhao, C. Liu, D.-M. Tang, M. Cheng, F. Zhang, H.-M. Cheng, *Energy Environ. Sci.* 9 (2016) 3079–3084.
- [27] M.S. Faber, R. Dziedzic, M.A. Lukowski, N.S. Kaiser, Q. Ding, S. Jin, *J. Am. Chem. Soc.* 136 (2014) 10053–10061.
- [28] J. Qin, S. Zhu, C. Feng, N. Zhao, C. Shi, E.-Z. Liu, F. He, L. Ma, J. Li, C. He, *Appl. Surf. Sci.* 433 (2018) 568–574.
- [29] Y. Xu, G. Shi, X. Duan, *Acc. Chem. Res.* 48 (2015) 1666–1675.
- [30] X. Wang, Q. Liu, J. Liu, R. Chen, H. Zhang, R. Li, Z. Li, J. Wang, *Appl. Surf. Sci.* 426 (2017) 1063–1074.
- [31] Y. Zhao, X. Xie, J. Zhang, H. Liu, H.-J. Ahn, K. Sun, G. Wang, *Chem. Eur. J.* 21 (2015) 15908–15913.
- [32] J. Sha, C. Gao, S.K. Lee, Y. Li, N. Zhao, J.M. Tour, *ACS Nano* 10 (2016) 1411–1416.
- [33] T. Cheng, B. Yu, L. Cao, H. Tan, X. Li, X. Zheng, W. Li, Z. Ren, J. Bai, *J. Colloid Interf. Sci.* 501 (2017) 1–10.
- [34] W. Zhou, K. Zhou, D. Hou, X. Liu, G. Li, Y. Sang, H. Liu, L. Li, S. Chen, *ACS Appl. Mater. Interfaces* 6 (2014) 21534–21540.
- [35] W. Wang, J. Yu, Q. Xiang, B. Cheng, *Appl. Catal. B: Environ.* 119–120 (2012) 109–116.
- [36] H. Zou, B. He, P. Kuang, J. Yu, K. Fan, *Adv. Funct. Mater.* 28 (2018) 1706917.
- [37] L.M. Chen, Y.N. Liu, *ACS Appl. Mater. Interfaces* 3 (2011) 3091–3096.
- [38] W. Zhou, J. Zhou, Y. Zhou, J. Lu, K. Zhou, L. Yang, Z. Tang, L. Li, S. Chen, *Chem. Mater.* 27 (2015) 2026–2032.
- [39] P. Kuang, B. Zhu, Y. Li, H. Liu, J. Yu, K. Fan, *Nanoscale Horiz.* 3 (2018) 317–326.
- [40] Y. Liu, H. Zhang, J. Ke, J. Zhang, W. Tian, X. Xu, X. Duan, H. Sun, M.O. Tade, S. Wang, *Appl. Catal. B: Environ.* 228 (2018) 64–74.
- [41] J.W. Miao, F.X. Xiao, H.B. Yang, S.Y. Khoo, J.Z. Chen, Z.X. Fan, Y.Y. Hsu, H.M. Chen, H. Zhang, B. Liu, *Sci. Adv.* 1 (2015) e1500259.
- [42] H. Zhu, J. Zhang, R. Yanzhang, M. Du, Q. Wang, G. Gao, J. Wu, G. Wu, M. Zhang, B. Liu, J. Yao, X. Zhang, *Adv. Mater.* 27 (2015) 4752–4759.
- [43] Y. Liu, X. Xu, J. Zhang, H. Zhang, W. Tian, X. Li, M.O. Tade, H. Sun, S. Wang, *Appl. Catal. B: Environ.* 239 (2018) 334–344.
- [44] C. Huang, T. Ouyang, Y. Zou, N. Li, Z.-Q. Liu, *J. Mater. Chem. A* 6 (2018) 7420–7427.
- [45] H. Zou, B. He, P. Kuang, J. Yu, K. Fan, *ACS Appl. Mater. Interfaces* 10 (2018) 22311–22319.
- [46] C. Wu, B. Liu, J. Wang, Y. Su, H. Yan, C. Ng, C. Li, J. Wei, *Appl. Surf. Sci.* 441 (2018) 1024–1033.
- [47] J. Jiang, M. Gao, W. Sheng, Y. Yan, *Angew. Chem. Int. Ed.* 55 (2016) 15240–15245.
- [48] W. Lai, Y. Xu, Y. Ren, L. Yang, J. Zheng, X. Yi, W. Fang, *Catal. Sci. Technol.* 6 (2016) 497–506.
- [49] F. Xu, L. Zhang, B. Cheng, J. Yu, *ACS Sustain. Chem. Eng.* 6 (2018) 12291–12298.
- [50] Y. Tang, Y. Wang, X. Wang, S. Li, W. Huang, L. Dong, C. Liu, Y. Li, Y. Lan, *Adv. Energy Mater.* 6 (2016) 1600116.
- [51] T. Liu, C. Jiang, B. Cheng, W. You, J. Yu, *J. Mater. Chem. A* 5 (2017) 21257–21265.
- [52] J.-Y. Wang, T. Ouyang, N. Li, T. Ma, Z.-Q. Liu, *Sci. Bull.* 63 (2018) 1130–1140.
- [53] K. Xiao, L.X. Ding, G. Liu, H. Chen, S. Wang, H. Wang, *Adv. Mater.* 28 (2016) 5997–6002.
- [54] X. Liu, I.S. Amiinu, S. Liu, Z. Pu, W. Li, B. Ye, D. Tan, S. Mu, *Adv. Mater. Interfaces* 4 (2017) 1601227.
- [55] B. Zhu, C. Qu, S. Gao, Z. Liang, H. Zhang, R. Zou, *ChemCatChem* 10 (2018) 1113–1121.
- [56] S. Ratso, I. Kruusenberg, M. Vikkisk, U. Joost, E. Shulga, I. Kink, T. Kallio, K. Tammeveski, *Carbon* 73 (2014) 361–370.
- [57] M. Rahsepar, M.R. Nobakht, H. Kim, M. Pakshir, *Appl. Surf. Sci.* 447 (2018) 182–190.
- [58] W. Qin, L. Han, H. Bi, J. Jian, X. Wu, P. Gao, *Nanoscale* 7 (2015) 20180–20187.
- [59] Y. Song, S. Bai, L. Zhu, M. Zhao, D. Han, S. Jiang, Y.N. Zhou, *ACS Appl. Mater. Interfaces* 10 (2018) 13606–13613.
- [60] A. Sivanantham, P. Ganesan, S. Shanmugam, *Adv. Funct. Mater.* 26 (2016) 4661–4672.
- [61] C. Guan, X. Liu, A.M. Elshahawy, H. Zhang, H. Wu, S.J. Pennycook, J. Wang, *Nanoscale Horiz.* 2 (2017) 342–348.
- [62] J. Wang, H. Zhong, Z. Wang, F. Meng, X. Zhang, *ACS Nano* 10 (2016) 2342–2348.
- [63] P. Ganesan, A. Sivanantham, S. Shanmugam, *J. Mater. Chem. A* 4 (2016) 16394–16402.
- [64] J. Ma, L. Liu, Q. Chen, M. Yang, D. Wang, Z. Tong, Z. Chen, *Appl. Surf. Sci.* 399 (2017) 535–541.
- [65] Y. Liang, Y. Li, H. Wang, H. Dai, *J. Am. Chem. Soc.* 135 (2013) 2013–2036.
- [66] Y. Li, H. Wang, L. Xie, Y. Liang, G. Hong, H. Dai, *J. Am. Chem. Soc.* 133 (2011) 7296–7299.
- [67] W. Zhu, X. Yue, W. Zhang, S. Yu, Y. Zhang, J. Wang, *J. Chem. Commun.* 52 (2016) 1486–1489.
- [68] D. Liu, Q. Lu, Y. Luo, X. Sun, A.M. Asiri, *Nanoscale* 7 (2015) 15122–15126.
- [69] L. Jiao, Y.-X. Zhou, H.-L. Jiang, *Chem. Sci.* 7 (2016) 1690–1695.
- [70] B. Zhang, C. Xiao, S. Xie, J. Liang, X. Chen, Y. Tang, *Chem. Mater.* 28 (2016) 6934–6941.